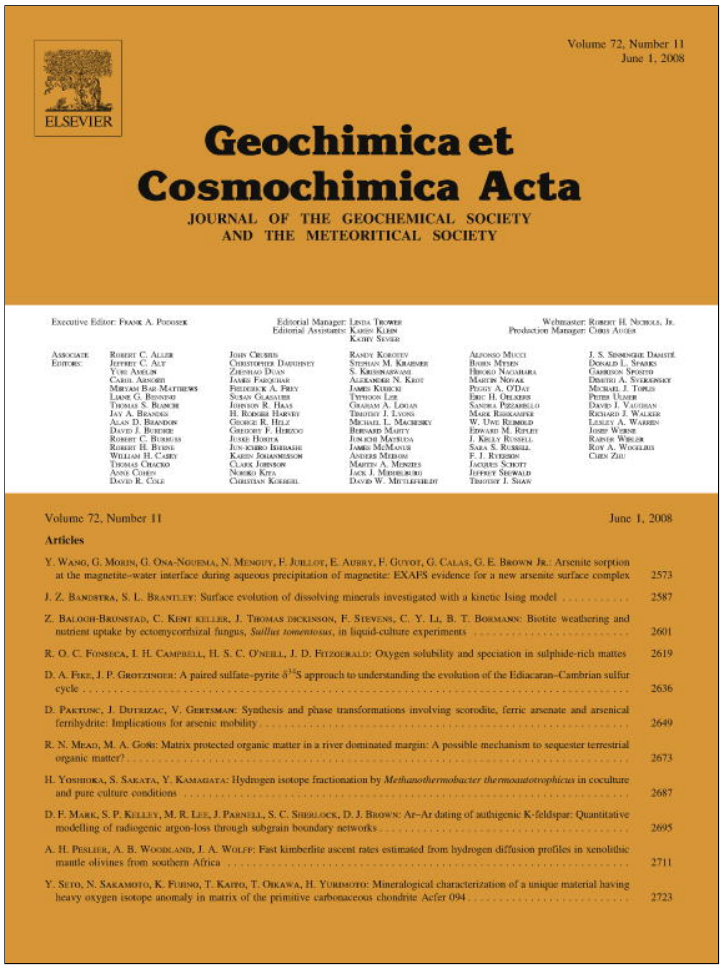

Volume 72, Number 11
June 1, 2008

ELSEVIER

Geochimica et Cosmochimica Acta

JOURNAL OF THE GEOCHEMICAL SOCIETY
AND THE METEORITICAL SOCIETY

Volume 72, Number 11 June 1, 2008

Articles

Available online at www.sciencedirect.com
ScienceDirect
Geochimica et Cosmochimica Acta 72 (2008) 2573–2586
Geochimica et Cosmochimica Acta
www.elsevier.com/locate/gca

Arsenite sorption at the magnetite–water interface during aqueous precipitation of magnetite: EXAFS evidence for a new arsenite surface complex

Yuheng Wang [a], Guillaume Morin [a,*], Georges Ona-Nguema [a], Nicolas Menguy [a], Farid Juillot [a], Emmanuel Aubry [b], François Guyot [a], Georges Calas [a], Gordon E. Brown Jr. [c,d]

[a] *Institut de Minéralogie et de Physique des Milieux Condensés (IMPMC), UMR 7590, CNRS, UPMC, UDD, IPGP, 140, rue de Lourmel, 75015 Paris, France*
[b] *Biogéochimie et Ecologie des Milieux Continentaux (Bioemco), UMR 7618 Université Paris 6, INRA, INAPG, CNRS, ENS, ENSCP Case 120, Tour 56, couloir 56–66, 4ème étage. 4 place Jussieu, 75252 Paris cedex 05, France*
[c] *Surface & Aqueous Geochemistry Group, Department of Geological and Environmental Sciences, Stanford University, Stanford, CA 94305-2115, USA*
[d] *Stanford Synchrotron Radiation Laboratory, SLAC, 2575 Sand Hill Road, MS 69, Menlo Park, CA 94025, USA*

Received 17 August 2007; accepted in revised form 9 March 2008; available online 1 April 2008

Abstract

The interaction of aqueous As(III) with magnetite during its precipitation from aqueous solution at neutral pH has been studied as a function of initial As/Fe ratio. Arsenite is sequestered via surface adsorption and surface precipitation reactions, which in turn influence the crystal growth of magnetite. Sorption samples were characterized using EXAFS spectroscopy at the As K-edge in combination with HRTEM observations, energy dispersive X-ray analysis at the nanoscale, electron energy loss spectroscopy at the Fe L_3-edge, and XRD-Rietveld analyses of reaction products. Our results show that As(III) forms predominantly tridentate hexanuclear As(III)O_3 complexes (^3C), where the As(III)O_3 pyramids occupy vacant tetrahedral sites on {1 1 1} surfaces of magnetite particles. This is the first time such a tridentate surface complex has been observed for arsenic. This complex, with a dominant As–Fe distance of 3.53 ± 0.02 Å, occurs in all samples examined except the one with the highest As/Fe ratio (0.33). In addition, at the two highest As/Fe ratios (0.133 and 0.333) arsenite tends to form mononuclear edge-sharing As(III)O_3 species (^2E) within a highly soluble amorphous As(III)–Fe(III,II)-containing precipitate. At the two lowest As/Fe ratios (0.007 and 0.033), our results indicate the presence of additional As(III) species with a dominant As–Fe distance of 3.30 ± 0.02 Å, for which a possible structural model is proposed. The tridentate ^3C As(III)O_3 complexes on the {1 1 1} magnetite surface, together with this additional As(III) species, dramatically lower the solubility of arsenite in the anoxic model systems studied. They may thus play an important role in lowering arsenite solubility in putative magnetite-based water treatment processes, as well as in natural iron-rich anoxic media, especially during the reductive dissolution-precipitation of iron minerals in anoxic environments.

1. INTRODUCTION

Magnetite is a common magnetic iron oxide in the lithosphere, pedosphere, and biosphere (Cornell and Schwertmann, 2003). In ambient temperature Earth surface environments, magnetite often forms via bacterial activity in aquifers, soils, and sediments. Under microaerophilic conditions, magnetotactic bacteria produce intracellular magnetite, which could serve as a potential biosignature in rocks (Thomas-Keprta et al., 2000; Golden et al., 2004). Under anoxic conditions, iron-reducing bacteria

* Corresponding author.
E-mail address: guillaume.morin@impmc.jussieu.fr (G. Morin).

0016-7037/$ - see front matter © 2008 Elsevier Ltd. All rights reserved.
doi:10.1016/j.gca.2008.03.011

can induce the formation of extracellular magnetite via dissimilatory reduction of ferric-oxyhydroxides (Lovley et al., 1987; Cooper et al., 2000; Ona-Nguema et al., 2001; Ona-Nguema et al., 2002; Glasauer et al., 2003). During iron and arsenic bioreduction in anoxic media, which is thought to be responsible for arsenic contamination of groundwaters in various localities, especially in Southeast Asia (e.g., Horneman et al., 2004; Polizzotto et al., 2005, 2006), neoformed, fine-grained magnetite, as well as other Fe(II)-bearing minerals (Larsen and Postma, 2001; Hansel et al., 2003; Hansel et al., 2005), can potentially influence the mobility of toxic trace elements such as arsenic via sorption and coprecipitation processes. Fine-grained magnetite is especially efficient at adsorbing As(III), the most toxic form of arsenic (Dixit and Hering, 2003), and its use for arsenic decontamination of water has been proposed based on its magnetic properties (Yavuz et al., 2006). However, little is known about the mechanism of interaction of dissolved As(III) with magnetite, especially during sorption and coprecipitation reactions. Based on X-ray absorption spectroscopy analysis, Coker et al. (2006) proposed that As(III) adsorbs onto the surface of neoformed magnetite upon dissimilatory reduction of arsenic-bearing ferrihydrite; however, the structure(s) and mode(s) of adsorption of the surface complex(es) were not determined. The objectives of the present study are to investigate the fate of As(III) during aqueous precipitation of magnetite and to evaluate the effect of As(III) on magnetite nucleation and growth processes as a function of the initial As(III)/Fe ratio in the aqueous medium. The mineralogy of the samples, including size, shape, and composition of the magnetite particles, and the oxidation state of iron, was characterized by coupling high-resolution transmission electron microscopy (HRTEM), energy dispersive X-ray analysis at the nanoscale, electron energy loss spectroscopy (EELS) at the Fe L_3-edge, and X-ray Rietveld analysis. The local environment of arsenic was determined by extended X-ray absorption fine structure (EXAFS) spectroscopy at the As K-edge. Our results show that As(III) forms a relatively soluble amorphous surface precipitate as well as several types of surface complexes, which lower the availability of As(III) in the anoxic systems studied and significantly influence the size of magnetite crystals, they also provide insights to the behavior of arsenite during magnetite precipitation in reducing environments.

2. MATERIALS AND EXPERIMENTAL DETAILS

2.1. Sample preparation

We prepared a series of magnetite samples with the following As(III)/Fe molar ratios: 0, 0.007, 0.033, 0.067, 0.133, and 0.333; these samples are referred to as MtAs0, MtAs0.007, MtAs0.033, MtAs0.067, MtAs0.133, and MtAs0.333, respectively. The synthesis was performed in a JACOMEX® glove box under N_2 atmosphere (<20 ppm O_2). All reagents were reagent grade (>99.9% purity level), and the solutions were prepared in the glove box with O_2-free milli-Q water. Samples were prepared by aqueous coprecipitation of Fe^{2+} and Fe^{3+} ions in the presence of various quantities of H_3AsO_3 ions by adding selected volumes of 1 M $NaAsO_2$ solution to serum bottles containing 5 mL of 1 M $FeCl_2{\cdot}4H_2O$ solution and 10 mL of 1 M $FeCl_3{\cdot}6H_2O$ solution. The pH was then adjusted to 7.2 by adding appropriate quantities of 1 M NaOH solution. The final ionic strength of the solutions ranged from 0.7 to 1 M. Each flask was sealed with butyl rubber stoppers and was agitated for 24 h at 25 °C. The suspension was then centrifuged, and the resulting black powder was dried under vacuum in the glove box for later X-ray diffraction (XRD) analysis, high-resolution transmission electron microscopy (HRTEM), and energy dispersive X-ray spectroscopy (EDXS) analysis. The supernatant was filtered through a 0.22 μm cellulose membrane, acidified to pH 1 with HNO_3, and stored in the glove box until further solution analysis.

Two reference samples were also prepared. An Fe(III)–As(III)-containing coprecipitate was synthesized as described above, with an As(III)/Fe(III) ratio of 0.5, in the absence of Fe(II) in the aqueous medium. A sample of As(III) adsorbed on magnetite, referred to as As(III)/Mt, was synthesized at the same pH as the coprecipitates studied here (pH 7.2), using sample MtAs0 as the substrate and an As/Fe ratio of 0.010. In preparing this sample, 0.5 g of magnetite powder (MtAs0) was suspended in a serum bottle with 0.1 M NaCl solution. Then, 1.0 mL of 0.0668 M $NaAsO_2$ was added, and the pH was adjusted to 7.2 by adding an appropriate quantity of 1 M NaOH solution. The final ionic strength of this solution was 0.1 M. The sample was then treated in the same way as the Fe(III)–As(III)-containing coprecipitation sample. Assuming a surface area of $103 \pm 3\ m^2\ g^{-1}$ calculated from the mean coherent dimension (MCD) value (Table 1), the As surface loading determined by analyzing the supernatant was $1.3 \pm 0.1\ \mu mol\ m^{-2}$ after a reaction time of 24 h.

2.2. Aqueous phase analysis

The supernatants were filtered through a 0.22 μm membrane and acidified to pH 1 with HNO_3 in the glove box to avoid precipitation of iron oxides that would cause a decrease in concentration of iron and arsenic in the solution. Fe concentrations were determined by inductively coupled plasma–atomic emission spectroscopy (ICP–AES) performed on a Jobin-Yvon® JY 238 Ultrace spectrometer, and As concentrations were determined by graphite furnace atomic absorption spectrometry (GFAAS) on a Unicam® 989 QZ spectrometer. The detection limits were 0.018 and 0.03 μM for Fe and As, respectively.

2.3. Electron microprobe analysis (EMPA)

The concentration of arsenic in the solid samples was measured by electron microprobe analysis at the Centre d'Analyses par Microsonde Electronique de Paris (Université Paris 6) using an SX50 CAMECA electron microprobe equipped with four wavelength dispersive spectrometers, operating at 20 kV and 40 nA, with a counting time of 10 s per point for measuring As. Twenty point analyses were averaged for each sample.

Table 1
Composition of the dissolved and solid phases in the As(III)-magnetite experiments

Sample	$[Fe]_{initial}$ [a] (mM)	$[As]_{initial}$ [a] (mM)	$[As]_{final}$ [b] (μM)	$[Fe]_{final}$ [c] (μM)	$[As]_{solid}$ [d] (wt%)	a (Å)	FWHM [e] (°2θ)	MCD [f] (nm)	SA [g] ($m^2\,g^{-1}$)	Γ [h] ($\mu mol\,m^{-2}$)
MtAs0	375	—	—	13720(50)	0	8.397(8)	0.82(2)	11.3(3)	103(3)	
MtAs0.007	375	2.2	<0.03	360(10)	1.1(1)	8.393(7)	0.71(1)	13.0(2)	90(1)	0.8(1)
MtAs0.033	375	11.2	0.3(1)	<0.03	3.0(4)	8.401(6)	0.75(1)	12.3(2)	95(1)	4.1(1)
MtAs0.067	375	22.3	11.0(5)	0.6(1)	5.3(2)	8.40(1)	1.61(3)	5.7(1)	203(4)	3.8(3)
MtAs0.133	375	44.6	93.0(5)	0.7(1)	9.9(7)	8.40(5)	2.9(2)	3.2(2)	366(25)	4.2(6)
MtAs0.333	375	112	31600(50)	2.0(1)	19.4(11)	n.m.	n.m.	n.m.	n.m.	n.m.
As(III) sorbed on MtAs0	0.6(1)[c]	1.7	40.0(5)	3.2(1)	2.3(0.1)	8.397(8)	0.82(2)	11.3(3)	103(3)	1.3(1)

Final pH is 7.2(±0.1) for all experiments. Estimated standard deviations (1σ) are given in parentheses and refer to the last digit.
n.m., not measurable.
[a] Calculated from the added quantity.
[b] Graphite furnace atomic absorption spectrometry (GFAAS) analysis.
[c] ICP–AES analysis.
[d] Electron microprobe analysis (EMPA).
[e] FWHM, full width at half maximum of Bragg peaks at 0° $2q$ corresponding to H_{L2} in Eq. (1), determined from Rietveld refinement.
[f] MCD, mean coherent dimension calculated from FWHM (see text).
[g] SA, surface area calculated from MCD values assuming spherical particle shape.
[h] Γ: apparent surface coverage determined from the analysis of the supernatant and assuming that the whole solid consists of magnetite with a surface area [g] calculated from MCD values.

2.4. X-ray diffraction (XRD)

To avoid oxidation by air, each powder sample was loaded into a glass capillary of 0.5 mm diameter, and the capillary was sealed with Superglue® under a N_2 atmosphere in the glove box ($O_2 \leqslant 20$ ppm). XRD measurements were performed with Co*Ka* radiation on a Panalytical® X'Pert Pro MPD diffractometer mounted in Debye–Scherrer configuration using an elliptical mirror to obtain a high flux parallel incident beam and an X'Celerator® detector to collect the diffracted beam. Data were recorded in the continuous-scan mode within the 5–80°2θ range with a step of 0.0167°. Diffraction patterns of samples MtAs0.067, MtAs0.133, and MtAs0.333 were recorded in 48 h, and XRD patterns of samples MtAs0, MtAs0.007, and MtAs0.033 were recorded in 12 h and were normalized in intensity to the previously obtained diffraction patterns by multiplying the latter by a factor of 4.

X-ray powder diffraction patterns were analyzed by the Rietveld method using the XND 1.3 program (Berar, 1990). Absorption through the capillary was corrected using a μx value of 1.5. A mixture of Gaussian and Lorentzian line shapes was used, and the Voigt profile shape function had the following form:

$$H_G^2 = H_{G1}^2 + \left(\frac{H_{G2}}{\cos\theta} + H_{G3}\cdot\tan\theta\right)^2 \quad \text{and} \quad H_L = H_{L1} + \frac{H_{L2}}{\cos\theta} + H_{L3}\cdot\tan\theta \tag{1}$$

where H_{G1} and H_{L1} are instrumental widths, H_{G2} and H_{L2} are related to the size broadening, and H_{G3} and H_{L3} are related to strain broadening. For the samples studied, H_{G3}, H_{L3}, and H_{G2} were found to be negligible, indicating a Lorentzian line shape, dominated by size broadening. The mean crystallite dimension was estimated from H_{L2}, using the Scherrer formula, $H(2\theta) = \frac{0.9\cdot\lambda}{L\cdot\cos\theta}$, where λ is the wavelength of the incident X-ray, 1.7902 Å for Co*Ka* in our case.

2.5. High-resolution transmission electron microscopy (HRTEM) and energy dispersive X-ray spectroscopy (EDXS)

Samples were prepared in the glove box using freshly prepared, dilute suspensions in absolute ethanol, dispersed by ultrasonication for 10–15 s. These suspensions were loaded into individual serum flasks sealed with butyl rubber stoppers and immediately taken to the electron microscope. Samples were then deposited onto carbon-coated grids using syringes and needles from the serum flasks. The grids were immediately transferred into the vacuum chamber of the electron microscope, and subsequent pump-down of the chamber resulted in evaporation of the suspension. Using this protocol, sample oxidation was assumed to be negligible. HRTEM images, EELS spectra, and EDXS spectra were taken using a JEOL® 2100F TEM. HRTEM images were recorded for about 50 particles in each sample. HRTEM images were processed using the ImageJ 1.34r program package (Choi et al., 2007).

2.6. XAFS data collection

XAFS data on vacuum-dried samples were recorded at the As K-edge (11,869 eV) using Si(220) double-crystal monochromator on beamline 11–2 at the Stanford Synchrotron Radiation Laboratory (SSRL). All data were collected in fluorescence detection mode using a 30 element Ge array detector. Elastic scattering and Fe fluorescence were minimized using a 3 $\Delta\mu$ Ge filter. Energy resolution was around 0.4–0.5 eV, with a vertical beam width of 250 μm^2, which was achieved using focusing mirrors. The horizontal beam width was limited to 500 μm using vertical slits. Energy was calibrated by using a double-transmission setup in which the As K-edge spectrum of the samples and that of a scorodite, $FeAsO_4{\cdot}2(H_2O)$ reference sample were simultaneously recorded. The absorption maximum of the As(V)-edge was chosen at 11,8725.0 eV.

Photo-oxidation of As(III) under the X-ray beam (Ona-Nguema et al., 2005) was limited by recording all data at 10–15 K using a modified Oxford® liquid He cryostat. In order to preserve anoxic conditions, the samples were transferred from the glove box to a liquid nitrogen bath and then to the cryostat where they were placed in a He atmosphere. Between 4 and 8 EXAFS scans were accumulated for each sample in order to obtain an adequate signal-to-noise ratio at $k_{max} = 14.5$ Å^{-1}. Samples were automatically moved 1 mm between each EXAFS scan since repeated scans on the same sample location might cause up to $7 \pm 2\%$ of As(III) to be oxidized after a 30 min EXAFS scan, which is below the EXAFS detection limit of mixed arsenic species (Cances et al., 2005).

2.7. EXAFS data analysis

EXAFS data were extracted using the XAFS program (Winterer, 1997) following the procedure detailed previously (Ona-Nguema et al., 2005). Radial distribution functions around the As absorber were obtained by calculating the Fourier transform (FT) of the $k^3\chi(k)$ EXAFS functions using a Kaiser–Bessel window within the 2.7–14.5 Å^{-1} k-range (except for the MtAs0.333 sample within the 2.7–12.3 Å^{-1} k-range because of poor data quality for this sample) with a Bessel weight of 2.5. Least-squares fitting of the unfiltered $k^3\chi(k)$ functions was performed with the plane-wave formalism, using a Levenberg–Marquard minimization algorithm. Theoretical phase-shift and amplitude functions employed in this fitting procedure were calculated with the curved-wave formalism using the ab initio FEFF 8 code (Ankudinov et al., 1998). As–O and As–Fe phase-shift and amplitude functions were extracted from the tooeleite structure (Morin et al., 2007) using FEFF 8.

The fit quality was estimated using a reduced χ^2 of the following form:

$$\chi^2_{FT} = \frac{N_{ind}}{(N_{ind} - p).n} \sum_{i=1}^{n} (\|FT\|_{exp_i} - \|FT\|_{calc_i})^2 \quad (2)$$

with N_{ind} (the number of independent parameters) $= (2\Delta k \Delta R)/(\pi)$, p the number of free fit parameters, n the number of data points fitted, and $\|FT\|_{exp}$ and $\|FT\|_{calc}$ the experimental and theoretical Fourier transform magnitude within the [0–8 Å] R-range of the k^3-weighted EXAFS. The number of allowable independent parameters is 59 ($\Delta k = 11.8$ and $\Delta R = 8$), and our fits included at most 16 variable parameters. A similar reduced χ^2 was calculated for the $k^3\chi(k)$ function and is referred to as χ^2.

3. RESULTS

3.1. Mineralogical composition of the samples

XRD analyses (Fig. 1) indicate that all samples except one (MtAs0.333) consist primarily of magnetite (Mt), with at least five detectable characteristic Bragg reflections [(220), (311), (400), (511), and (440)]. The exception (MtAs0.333) was a poorly defined amorphous phase with very broad lines slightly shifted with respect to the (311), (511), and (440) Bragg reflections of magnetite. Halite (NaCl) was present in all samples as a minor component, except for sample MtAs0.007, and served as an internal standard. Halite was a by-product of our magnetite synthesis procedure that used iron chloride and sodium hydroxide as starting reactants. Halite likely precipitated during vacuum drying of the final product so that no interference with magnetite nucleation and growth is expected. The capillary glass used as the sample container yielded a broad band at ~8.9°2θ.

Except for the most As-rich sample (MtAs0.333), no shift in Mt peak positions was observed from sample to sample. Rietveld analyses of all samples except MtAs0.333 indicate that the cell parameter of the spinel phase [$a \sim 8.40$ Å (see Table 1)] is consistent with that of magnetite ($a = 8.396$Å), and it is significantly larger than that of maghemite ($a = 8.347$Å) (Hill et al., 1979). In contrast, the full width at half maximum (FWHM) of the observed XRD lines significantly increase with increasing As(III)/Fe ratio, except for the MtAs0.007 sample which exhibits smaller FWHM than the MtAs0 control sample. The dominant Lorentzian shape of the observed peaks and the good match to a Scherrer broadening model ($H_{G2} = H_{G3} = H_{L3} = 0$ in Eq. (1); Table 1) indicate that the broadening of the XRD lines is mainly due to a decrease of the mean coherent dimension (MCD) of the magnetite crystallites in the samples studied. Surface areas calculated from these MCD values, assuming a spherical shape, vary from 90 ± 1 m^2 g^{-1} for sample MtAs0.007 to 366 ± 25 m^2 g^{-1} for sample MtAs0.133. Particle sizes determined by HRTEM observation of selected samples are consistent with Rietveld results and indicate that magnetite particle size decreases with increasing As(III)/Fe ratio (Table 1). In addition, TEM-determined particle sizes are consistent with this conclusion. Fifty particles of samples MtAs0 and MtAs0.007 measured using the TEM have mean diameters within the 5–15 nm range (Fig. 2a and b), whereas mean particle diameters for samples MtAs0.133 and MtAs0.333, are in the 3–5 nm range (Fig. 2c and d) and the 2–5 nm range (Fig. 2e), respectively. However, Mt crystal sizes for the samples with the lowest As(III) concentrations (MtAs0.007 and MtAs0.033) were found to be larger than that for the As-free sample (MtAs0) (Table 1). This exception to the inverse correlation between magnetite

particle size and As(III) concentration was confirmed by preparing and analyzing several replicates of the MtAs0, MtAs0.007, and MtAs0.033 samples and is addressed in Section 4.

HRTEM observations indicate that samples MtAs0 and MtAs0.007 mainly consist of cubo-octahedral shaped magnetite particles (Fig. 2a and b, respectively) displaying well-developed {1 1 1} crystallographic faces. With increasing As(III) concentration, the decrease in particle size makes it difficult to unambiguously determine their morphologies (samples MtAs0.133 and MtAs0.333 (Fig. 2c, d, and e)). A thin amorphous layer was detected on some of the surfaces of As-sorbed magnetite nano-particles samples except for those with the two lowest As/Fe ratios (MtAs0 and MtAs0.007; see Fig. 2a and b). This amorphous layer was found in sample MtAs0.067 (not shown) and is thicker in samples MtAs0.133 and MtAs0.333 (Fig. 2c, d, and e). The final concentration of dissolved iron decreased regularly with increasing initial arsenic concentration to <0.03 μM for sample MtAs0.033. For higher As concentrations, the dissolved iron concentration (e.g., 2.0 ± 0.1 μM for sample MtAs0.333) remains far below the value of the As-free sample (13270 ± 50 μM for sample MtAs0) (Table 1). This result suggests that, in addition to possible arsenic adsorption onto the magnetite particles, a fraction of arsenic and iron coprecipitated to form this amorphous layer. The composition of this coprecipitate was estimated by EDXS analysis of the amorphous layer in sample MtAs0.333 and it contains Fe and As in the As/Fe molar ratio of ~1 (Fig. 2f). EELS analysis of the amorphous layer suggests that the redox state of iron in the amorphous layer is similar to that in magnetite. Given the energy resolution

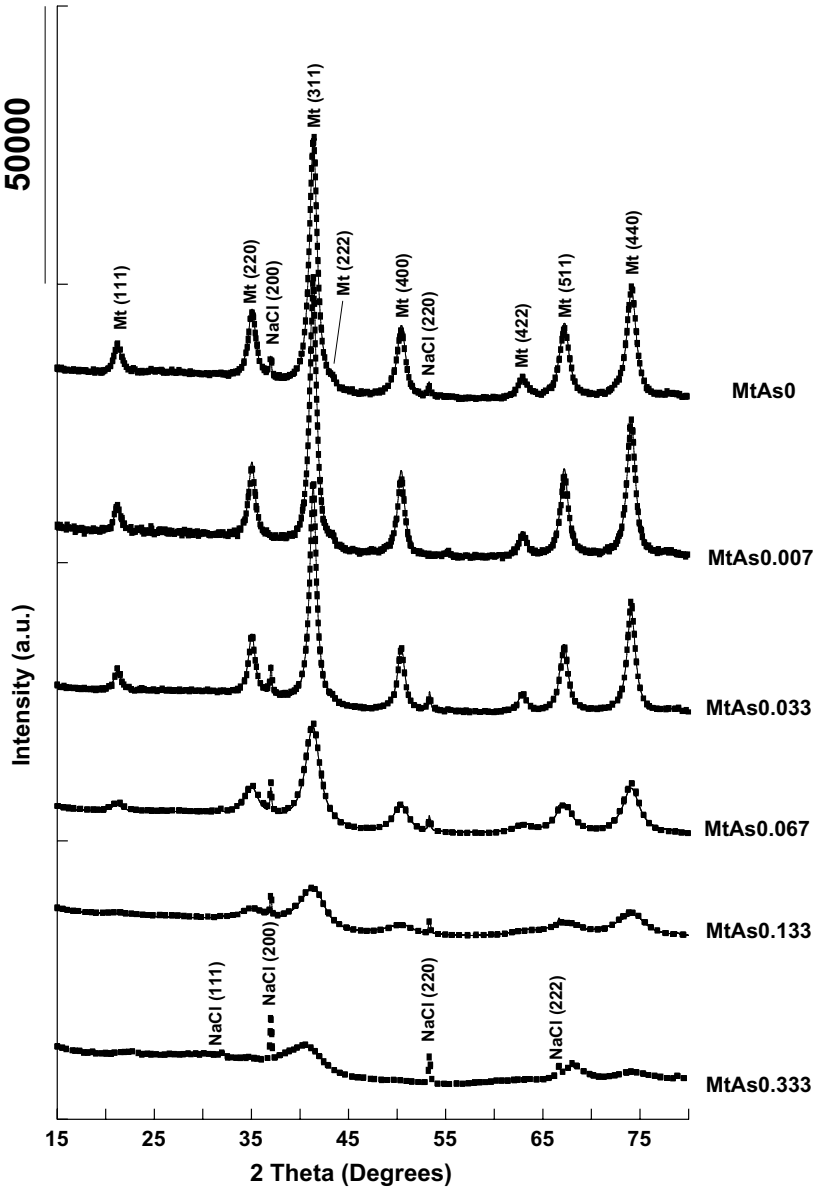

Fig. 1. Rietveld refinement of the X-ray powder diffraction patterns of the MtAs samples. Experimental: dashed lines; calculated: solid lines.

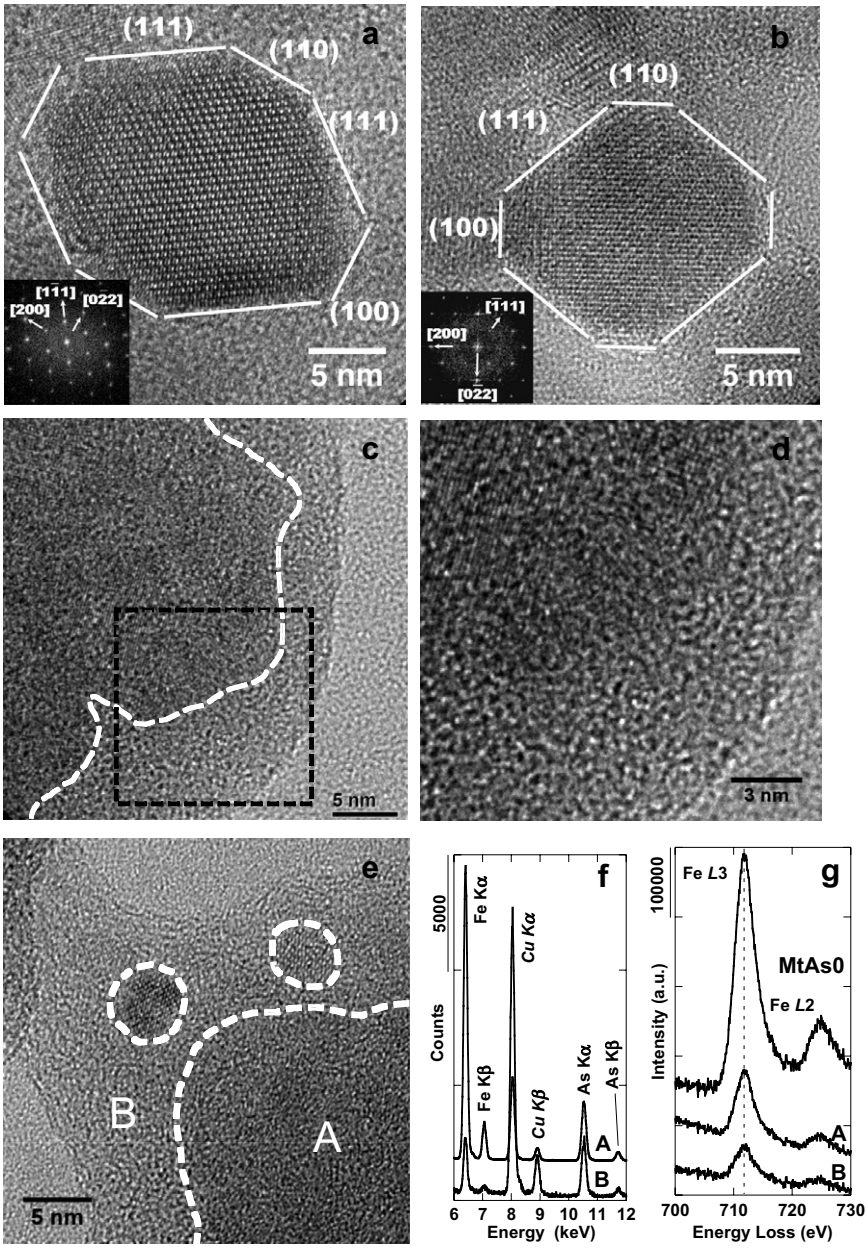

Fig. 2. HRTEM images of the MtAs samples. (a) Well-crystallized magnetite particle in the MtAs0 control sample and corresponding electron diffraction pattern along the [1 1 0] zone axis. Magnetite particles with cubo-octahedron morphology and well-developed {1 1 1} crystallographic faces are commonly observed. (b) Well-crystallized magnetite particle in the MtAs0.007 sample and corresponding electron diffraction pattern along the [1 1 0] zone axis. Magnetite particles with cubo-octahedral morphology and well-developed {1 1 1} crystallographic faces are commonly observed. (c) Aggregate in sample MtAs0.133 composed of nano-particles of magnetite in the size range 3–5 nm coated by an amorphous layer 3–10 nm thick. The boundary between the nano-particles and the amorphous layer is marked by a white dashed line. (d) Enlarged view of the area in Fig. 2c outlined by the black dashed line. Nano-magnetite particles can be distinguished from the amorphous layer by their lattice fringes. (e) Sample MtAs0.333, isolated and aggregated nano-particles of magnetite in the size range 2–5 nm embedded within an amorphous layer 3–10 nm thick. The boundary between the nano-particles and the amorphous layer is marked by a white dashed line. (f) EDXS spectra taken within zones A (nano-magnetite aggregate) and B (amorphous layer) displayed in Fig. 2e. Three repeated analyses in each zone indicated As/Fe molar ratio values of 0.4 ± 0.2 and 1.0 ± 0.3, respectively. (g) EELS spectra in zones A and B in Fig. 2e and from a particle of sample MtAs0, with a spot size of ~3 nm. For the three spectra, the energy position of the Fe L_3 maximum intensity occurs at 712.0 eV, as expected for magnetite (Gloter et al., 2003).

of our EELS data, a significant change in the iron redox state should have led to a shift in the energy loss maximum of the Fe L_3 peak (Gloter et al., 2003), which was not observed.

3.2. Arsenic oxidation state

Arsenic K-edge XANES data indicate that As(III) did not oxidize in any of the experiments. Indeed, XANES spectra of As(III)-sorbed samples exhibit a well-resolved edge structure with an absorption maximum at 11,871.3eV (not shown), corresponding to As(III) (Ona-Nguema et al., 2005). Although Fe(III) can oxidize As(III) to As(V) in solution, based on equilibrium thermodynamic data (Vanysek, 1995), our XANES results indicate that no observable change in arsenic oxidation state occurred in any of the sorption samples within 24 h. This result is consistent with those recently obtained by our group for As(III) sorption onto ferric-oxyhydroxides, which showed that As(III) did not oxidize in the presence of ferrihydrite, goethite, or lepidocrocite even after an equilibration time of 1 week under anoxic conditions (Ona-Nguema et al., 2005). Arsenic(III) is known to oxidize rapidly under oxic or microaerophilic conditions when Fenton reactions take place via reactive oxygen species (e.g., $O_2^{\cdot -}$, H_2O_2, $^{\cdot}OH$) formed as intermediate species during the oxidation of Fe(II) by dissolved O_2 (Hug and Leupin, 2003). In the present study, strict anoxic conditions prevented any As(III) oxidation by Fenton reactions.

3.3. EXAFS results: local environments of arsenic

Arsenic K-edge, unfiltered, k^3-weighted EXAFS data for the samples are displayed in Fig. 3a, and those for two reference compounds are shown in Fig. 3c. The corresponding Fourier tansforms are shown in Fig. 3b and d. The spectra of MtAs0.033, MtAs0.067, and MtAs0.133 exhibit strong similarities, and differ from those of MtAs0.007 and MtAs0.333. Tables 2 and 3 list the results of fitting the unfiltered $k^3\chi$(k) EXAFS functions. First-neighbor contributions were fit with 2.7–3.2 oxygen atoms at 1.78 ± 0.02 Å (Table 3), corresponding to the AsO_3 pyramidal threefold coordination. In all samples, second-neighbor contributions to the EXAFS were fit using As–Fe pairs at various distances and a multiple scattering contribution corresponding to the six As–O–O paths within the AsO_3 pyramid (Fig. 3a and b, and Table 3). The number of multiple scattering paths was fixed at the expected value of 6. The distances fit for this contribution in our samples ranged from 3.15 to 3.22 Å, and thus they are consistent with the corresponding As–O–O multiple scattering path in the structure of tooeleite (3.14 Å) (Morin et al., 2007).

The EXAFS spectra of samples MtAs0.007, MtAs0.033, MtAs0.067, and MtAs0.133 exhibit sharp second-neighbor contributions, as well as significant contributions from neighbors at longer distances (Fig. 3b). Second-neighbor contributions for samples MtAs0.033, MtAs0.067, and MtAs0.133 are similar (Fig. 3b), but they differ from those for sample MtAs0.007.

For sample MtAs0.007, two As–Fe pair correlations at 3.30 ± 0.02 and 3.49 ± 0.02 Å were observed (Fig. 3a and b, and Table 3). In contrast, for samples MtAs0.033, MtAs0.067, and MtAs0.133, the fits yielded a well-defined As–Fe pair correlation at 3.53 ± 0.02 Å and an additional one at 3.73 ± 0.02 Å (Fig. 3a and b, and Table 3). In sample MtAs0.333, the weak second-neighbor contribution was fit by 0.3 Fe atoms at 2.97 ± 0.03 Å (Fig. 3b and Table 3). This As–Fe distance is similar to that found for the XRD amorphous Fe(III)–As(III) coprecipitate model compound, although for this latter compound, an additional As–Fe pair correlation was fit at 3.37 ± 0.02 Å (Fig. 3d and Table 3).

Interestingly, the As–Fe pair correlations at 3.53 ± 0.02 and 3.73 ± 0.02 Å in samples MtAs0.033, MtAs0.067, and MtAs0.133 are, within estimated error, similar to those observed in the As(III)/magnetite sorption sample (Fig. 3d and Table 3). This similarity extends to more distant features in the FT at 4–7 Å, which are significant for all samples except the most concentrated one (sample MtAs0.333). Analysis of these long-distance contributions is detailed for sample MtAs0.067 in Fig. 4 and Table 2, and shows they are due to multiple scattering. Arsenic K-EXAFS data of this sample are consistent with ^{3}C tridentate hexanuclear As(III) surface complexes where the AsO_3 pyramid occupies a tetrahedral vacancy on the {1 1 1} surface of magnetite. The geometry of this proposed surface complex is displayed in Fig. 5a and b. Feff8 calculations show that major photoelectron multiple scattering paths expected from the proposed geometry compare well with the experimental data. Indeed, in addition to the As–Fe pair correlations at 3.53 ± 0.02 and 3.72 ± 0.02 Å, the fit result yields two main multiple scattering paths: As–O–Fe at 5.53 ± 0.05 Å and As–Fe–Fe–Fe at 6.97 ± 0.5 Å, and a minor single scattering As–Fe pair at 6.00 ± 0.5 Å, all of which are consistent with the proposed ^3C complex. Although the number of neighbors that can be determined from these longer distance contributions has lower least-squares precision and accuracy than the number of closer Fe neighbors, these longer distances have good precision (±0.05 Å); therefore, they can be used to propose this intermediate-range structure model. Contributions from all of these long paths are clearly observed in the FT's of the EXAFS spectra of the As(III)/Mt sorption sample (Fig. 3d), and most of them are observed in the FT's of samples MtAs0.033 and MtAs0.007 (Fig. 3b). They are much less intense in the FT of sample MtAs0.133 (Fig. 3b).

4. DISCUSSION

4.1. Molecular-level speciation of arsenic(III) at the magnetite–water interface

Our results indicate the formation of tridentate hexanuclear corner-sharing (^3C) As(III)O_3 complexes on the {1 1 1} facets of magnetite under the experimental conditions of this study. Such a surface complex, referred to as species (i) in Table 3 and in the following text, is displayed in Fig. 5a and b. It occurs in samples MtAs0.007, MtAs0.033, MtAs0.067, and MtAs0.133 as well as in the As(III)/Mt sorption sample. The dominant As–Fe pair correlation at 3.53 ± 0.02 Å, which is characteristic of the proposed ^3C complex on the magnetite surface, is similar to the single As–Fe pair correlation at 3.50 ± 0.05 Å recently observed by Coker et al. (2006) in their As(III)/Mt sorption sample, as well as in their Mt sample resulting from the bioreduc-

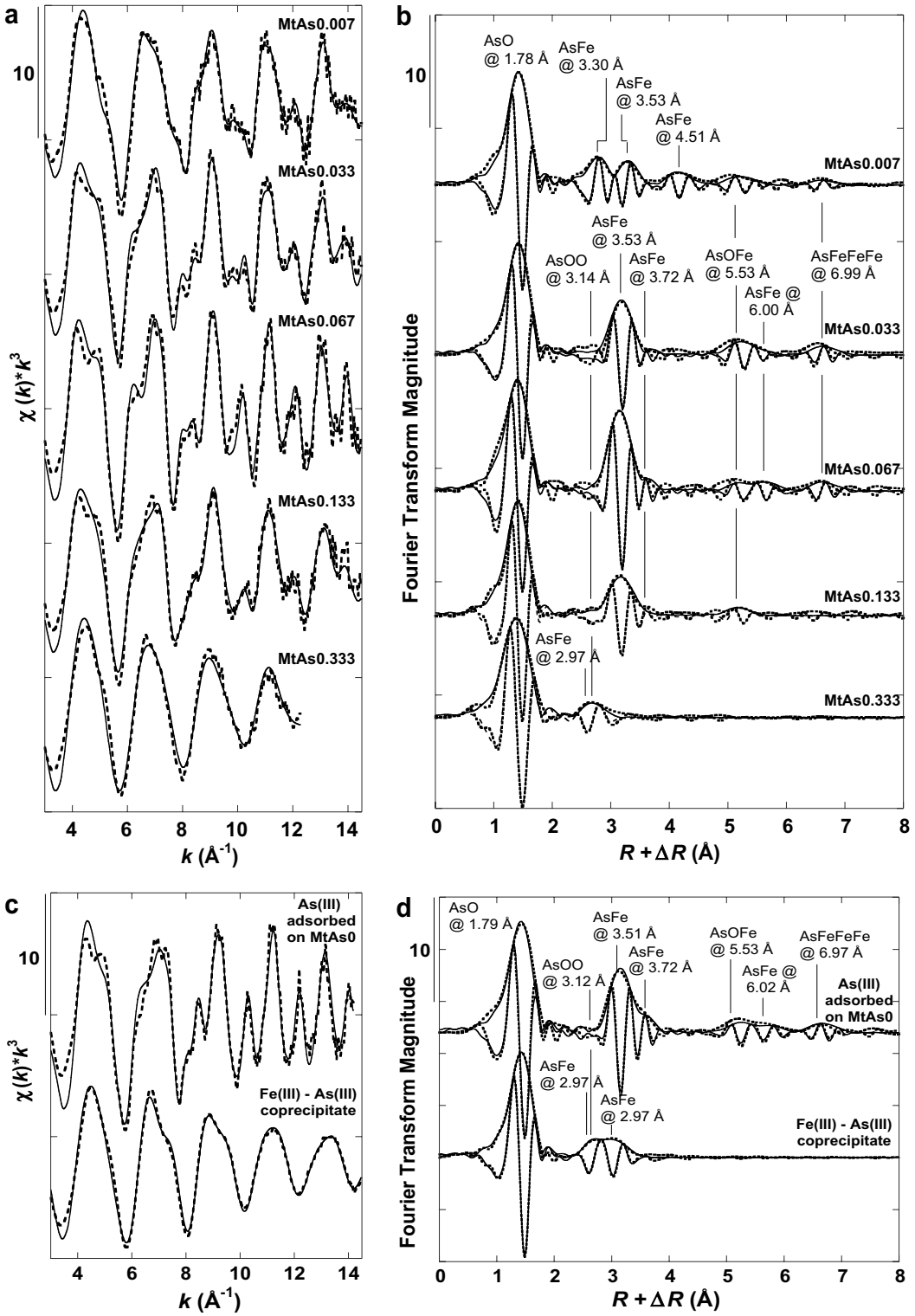

Fig. 3. As K-edge unfiltered EXAFS data recorded at 10 K for MtAs samples, the As(III) sorbed on magnetite sample, and the amorphous As(III)–Fe(II) co-precipitate: (a and c) k^3-weighed $\chi(k)$ EXAFS, and (b and d) their corresponding Fourier transforms (FT), including the magnitude and imaginary part of the FT. Experimental and calculated curves are displayed as dashed and solid lines, respectively. All fit parameters are provided in Table 3.

tion of As-doped ferrihydrite. Such a similar distance that differs from those generally observed for As(III) sorption complexes on other iron oxides, i.e. 2.9 and 3.4 Å for ^2E and ^2C complexes, respectively (Ona-Nguema et al., 2005

Table 2
EXAFS fitting results for sample MtAs0.067, compared with scattering paths expected for the proposed ^3C tridentate As(III) complexes on the {111} face

Scattering paths[a]	EXAFS MtAs0.067		^3C As(III) complex on the {111} face of magnetite		Tetrahedral Fe on the {111} face of magnetite[b]	
	R (Å)	N	R (Å)	N	R (Å)	N
O	1.79	3 As–O	1.79	3 As–O	1.89	4 Fe–O
A	3.53	4.6 As–Fe	3.52	6 As–Fe	3.48	6 Fe–Fe
B	3.72	1.9 As–Fe	3.72	1 Fe–Fe	3.63	1 Fe–Fe
C	5.53	1.8 As–O–Fe	5.48	8 As–Fe	5.45	8 Fe–Fe
				6 As–O–Fe		6 Fe–O–Fe
				3 As–O–Fe–O		3 Fe–O–Fe–O
D			5.50	2 As–Fe		
E	6.00	1.8 As–Fe	5.99	3 As–Fe	5.93	3 Fe–Fe
F	6.98	1.1 As–Fe–Fe–Fe	6.94	3 As–Fe	6.88	3 Fe–Fe
G			6.99	6 As–Fe	6.96	6 Fe–Fe
				12 As–Fe–Fe		12 Fe–Fe–Fe
				6 As–Fe–Fe–Fe		6 Fe–Fe–Fe–Fe

Dominant single and multiple scattering paths (O, A, B, C, D, E, F, G) were identified by a Feff8 calculation based on the structural model drawn in Fig. 5a and b. In this model, the position of the As atom and of its first-neighbor oxygen atoms has been adjusted by trial and error to approach the optimum geometry of the AsO_3 pyramid (As–O = 1.79 Å and O–As–O = 100° in As_2O_3) and to satisfy the observed As–Fe distance of 3.53 Å. The corresponding displacement of oxygen atoms belonging to Fe octahedra leads to a relaxation of the Fe–O distance of only 1%. The relative contributions to the EXAFS of the dominant single and multiple scattering paths corresponding to the proposed ^3C surface complex are displayed in Fig. 4 for sample MtAs0.067.

Note: R (Å), interatomic distances; N, number of neighbors; errors on R and N values, estimated from the fit of the tooeleite As K-edge EXAFS data (not shown), are ±0.02 and ±0.5 below $R = 4$ Å, ±0.05 and ±1.0 above $R = 4$ Å.

[a] Scattering paths shown in Fig. 5.

[b] Feff8 calculation based on the crystal structure from Hill et al. (1979), assuming a central Fe atom in tetrahedral site lying on the half of a crystal sliced along a (111) plane terminated by octahedral sites.

and references therein), suggests that the dominant speciation of arsenite in the As(III)/Mt samples prepared by Coker et al. corresponds to the ^3C surface complex we have proposed. Finally, the formation of this complex on the {111} surfaces of our fine particle magnetite is consistent with the octahedral termination of this surface, as recently proposed by Petitto et al. (2006) from single crystals surface X-ray diffraction analyses.

A second species, referred to as (ii), is characterized by a single As–Fe pair at 2.98 ± 0.03 Å that can be interpreted as a bidentate mononuclear edge-sharing surface complex (^2E). This dominant species in the most concentrated MtAs0.333 sample is likely related to the abundant amorphous surface precipitate coating magnetite particles that was observed by HRTEM in the same sample (Fig. 2e). HRTEM observations of our other samples indicated that species (ii) forms for initial As/Fe ratio of 0.067 and above and that its abundance increases with increasing initial arsenite concentration. The absence of the As–Fe pair correlation at 3.37 ± 0.02 Å in the MtAs0.333 sample, which is observed in the amorphous As(III)–Fe(III) model compound, suggests that the local structures of these amorphous compounds differ significantly. Such a difference could be related to the presence of both Fe(II) and Fe(III) in the amorphous coating and of only Fe(III) in the model compound.

A third species, referred to as species (iii) in Table 3 and in the following text, forms at low initial As concentration and is characterized by As–Fe distances of 3.30 and 4.51 Å, which are clearly observed in the FT's of sample MtAs0.007 and are observed to a lesser extent in the FT of sample MtAs.033. No suitable geometry for a surface complex matching these distances was found on the {111} surface of magnetite. Although the structural interpretation of such As–Fe distances is not unique, bidentate binuclear ^2C complexes (e.g., on {100} facets or steps of the magnetite particles) could account for such distances. The {100} surface of magnetite exhibits rows of FeO_6 octahedra with singly coordinated oxygens pointing outwards on either oxygen surface termination chosen. Such a ^2C complex would yield two As–Fe distances of 3.3 Å, which correspond to the binding of As(III) to singly coordinated oxygen atoms of two adjacent FeO_6 octahedra, and two As–Fe distances of 4.5 Å corresponding to the distance between As and the next tetrahedral Fe sites. According to such a model, the decreasing amount of species (iii) with increasing initial As(III) concentration could indicate that the number of available sites for this species (i.e., (100) facets or steps) decreases with increasing As/Fe ratio. Unfortunately this hypothesis cannot be verified by HRTEM analysis because the morphology of our fine magnetite particles cannot be unambiguously determined when increasing As(III) concentration. Other structural models could also be proposed to explain the set of distances characterizing species (iii), including the formation of As-bearing solid phases other than magnetite during the precipitation process at low As/Fe ratio. However, our HRTEM observations were unsuccessful in revealing the occurrence of such minor phases in samples MtAs0.007 and MtAs0.033.

Table 3
Results of shell-by-shell fitting of unfiltered EXAFS data for the MtAs samples, the As(III) sorbed on magnetite sample, and the amorphous As(III)–Fe(II) co-precipitate

Sample	R (Å)	N	σ (Å)	ΔE_0 (eV)	CHI^2_{FT}
MtAs0.007	1.79	2.8 As–O	0.05	14	0.08
	3.22	6.0(f) As–O–O	—	—	
	3.30[iii]	1.8 As–Fe	0.07	—	
	4.51[iii]	1.3 As–Fe	—	—	
	3.49[i]	1.8 As–Fe	—	—	
	5.56[i]	1.4 As–O–Fe	—	—	
	6.96[i]	0.6 As–Fe–Fe–Fe	—	—	
MtAs0.033	1.79	3.0 As–O	0.06	15	0.11
	3.18	6.0(f) As–O–O	—	—	
	3.54[i]	3.1 As–Fe	0.07(f)	—	
	3.73[i]	1.1 As–Fe	—	—	
	5.56[i]	1.8 As–O–Fe	—	—	
	5.94[i]	0.6 As–Fe	—	—	
	6.96[i]	1.0 As–Fe–Fe–Fe	—	—	
MtAs0.067	1.78	3.3 As–O	0.07	13	0.14
	3.15	6.0(f) As–O–O	—	—	
	3.53[i]	4.6 As–Fe	0.07	—	
	3.72[i]	1.9 As–Fe	—	—	
	5.53[i]	0.9 As–O–Fe	—	—	
	6.00[i]	1.8 As–Fe	—	—	
	6.98[i]	1.1 As–Fe–Fe–Fe	—	—	
MtAs0.133	1.78	2.9 As–O	0.06	13	0.1
	3.19	6.0(f) As–O–O	—	—	
	3.52[i]	1.9 As–Fe	0.07(f)	—	
	3.74[i]	0.4 As–Fe	—	—	
	5.53[i]	1.1 As–O–Fe	—	—	
MtAs0.333	1.77	3.0 As–O	0.07	15	0.08
	3.13	6.0(f) As–O–O	—	—	
	2.97[ii]	0.3 As–Fe	0.06	—	
As(III) adsorbed on MtAs0	1.79	3.2 As–O	0.06	17	0.13
	3.12	6.0(f) As–O–O	—	—	
	3.51[i]	3.8 As–Fe	0.06	—	
	3.72[i]	2.0 As–Fe	—	—	
	5.53[i]	1.3 As–O–Fe	—	—	
	6.02[i]	1.6 As–Fe	—	—	
	6.97[i]	1.2 As–Fe–Fe–Fe	—	—	
Fe(III)–As(III) coprecipitate	1.79	2.7 As–O	0.05	17	0.04
	3.19	6.0(f) As–O–O	—	—	
	2.94	0.3 As–Fe	0.07	—	
	3.37	0.9 As–Fe	—	—	

The fits indicate three groups of distances that are interpreted as corresponding to three types of surface complexes: (i) ^3C tridentate complex on the Mt {1 1 1} face. (ii) ^2E in amorphous As(III)–Fe(III,II) precipitate. (iii) A third species (see text).
Note: R (Å): interatomic distances; N, number of neighbors; σ (Å), Debye Waller factor, ΔE_0 (eV): difference between the user-defined threshold energy and the experimentally determined threshold energy, in electron volts; CHI^2_{FT}: goodness-of-fit (see text). During the fitting procedure, all parameter values indicated by (—) were linked to the parameter value placed above in the table and those followed by (f) were fixed. Errors on R and N values, estimated from the fit of the tooeleite As K-edge EXAFS data (not shown), are ± 0.02 and ± 0.5 below $R = 4$ Å, ± 0.05 and ± 1.0 above $R = 4$ Å. Errors on σ and ΔE_0 values are ± 0.01 and ± 3, respectively.

4.2. Influence of As(III) on the magnetite nucleation and growth process

Magnetite is often synthesized by aqueous precipitation of Fe^{3+} and Fe^{2+} ions (Mann et al., 1989; Tronc et al., 1992; Jolivet et al., 1994; Cornell and Schwertmann, 2003). Ionic strength and pH are known to control magnetite particle size (Vayssieres et al., 1998; Jolivet et al., 2002; Sun and Zeng, 2002; Faivre et al., 2004) and crystal morphology (Devouard et al., 1998; Faivre et al., 2005), and the effect of these solution variables on particle size has been modeled by Jolivet et al. (2004). The formation of magnetite is also influenced by other ions in solution, such as phosphate (Mann et al., 1989) and sucrose (Tamaura et al., 1979). Based on these past studies, the formation of surface species (i), (ii), and (iii) is thus expected to influence

the nucleation and growth of magnetite in the present study, as discussed below. Cubo-octahedral magnetite particles are the most common shapes observed in our HRTEM images of sample MtAs0, which slightly differ from the morphology of nano-magnetite prepared by Faivre et al. (2005) via coprecipitation of ferrous and ferric ions in aqueous solution. Indeed, Faivre et al. observed magnetite nano-particles with more regularly shaped {1 1 1} facets than in the present study. This difference may be due to the fact that the supersaturation was higher in the present study than in Faivre et al. (2005). The cubo-octahedral shape of the arsenite-free sample (MtAs0) is preserved at low arsenite concentration (sample MtAs0.007), whereas at higher As(III) concentrations, the particle morphologies become more and more irregular.

The XRD and HRTEM results also show that the particle size of the single-domain magnetite varies as a function of the initial arsenic concentration in the precipitation medium (Table 1). Foreign solutes are known to inhibit the growth of small crystals. For instance, Rose and co-workers (Rose et al., 1996, 1997) found that the presence of sulfate ($SO_4/Fe = 0.5$) had little effect on the outcome of the Fe-oxide synthesis, while a small quantity of phosphate ($PO_4/Fe = 0.05$) can modify the mineralogy as well as the size and structure of the Fe-oxide particles. In addition, Vayssieres et al. (1998) and Jolivet et al. (2002) have studied the effect of ionic strength (I) and pH on the formation of magnetite particles, showing that average particle size decreases from 12.5 nm at pH 8.5 and $I = 0.5$ M to 1.6 nm at pH 12 and $I = 3$ M. In the present study, the only variable affecting particle size is the As(III) concentration in the medium, since the reaction pH and the ionic strength are similar for all samples (pH 7.2, $I = 1.5$ M). Surprisingly, at low concentration, the presence of arsenite favors an increase in size of the magnetite particles. Indeed, the mean particle size in sample MtAs0.007 (13.0 nm) and in sample MtAs0.033 (12.3 nm) is slightly larger than that in the As-free sample MtAs0 (11.3 nm) (Table 1). In contrast, higher arsenic concentrations tend to result in a decrease of the mean size of the magnetite particles: from 12.3 nm for sample MtAs0.033 to 3.2 nm for sample MtAs0.133.

Such an effect could be explained by the hypothesis that the adsorption of As(III) on iron-(hydr)oxide nuclei (species (iii) and (i)) inhibits their further growth and dissolu-

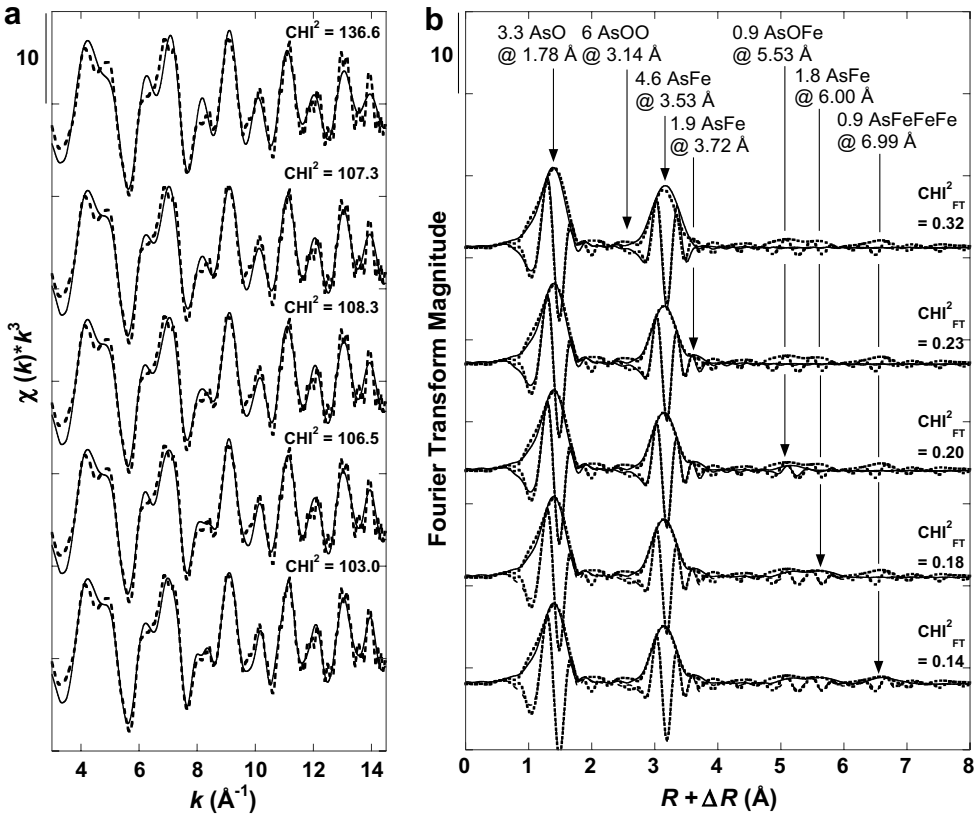

Fig. 4. As K-edge unfiltered EXAFS data recorded at 10 K for sample MtAs0.067 with different fit solutions: (a) k^3-weighed $\chi(k)$ EXAFS, and (b) its corresponding Fourier transforms (FT), including the magnitude and imaginary part of the FT. Experimental and calculated curves are displayed as dashed and solid lines, respectively. Form top to bottom, the first fit includes three scattering paths described in Table 2, and each successive fit includes one more scattering path than the previous. The values of the reduced χ^2 and χ^2_{FT} values (see text) significantly decrease when adding the shells corresponding to the ^3C tridentate As(III) complexes on the {1 1 1} face of magnetite (Table 2). The slight mismatch between the experimental and calculated EXAFS functions at low k values is due to single and multiple scattering by oxygen atoms at long distance. Theses paths were not included in the fit because of their very small contribution to the EXAFS, by comparison with the large number of fitting parameters required to fit them.

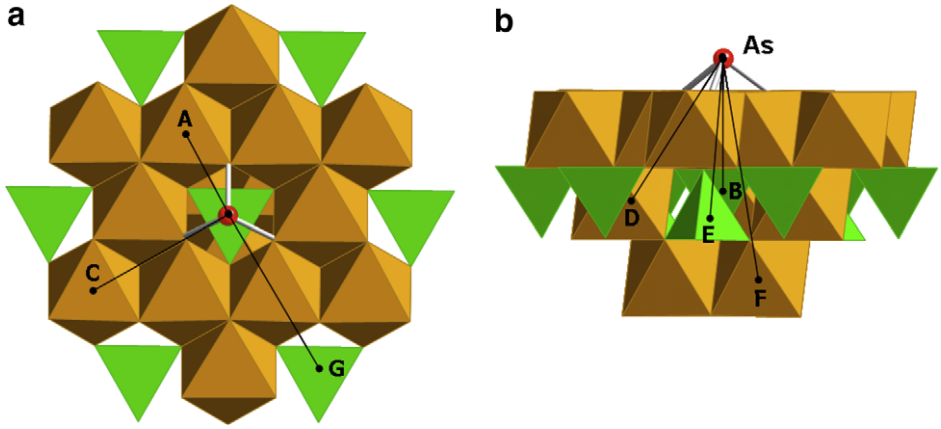

Fig. 5. (a) and (b) Proposed structural model for As(III) complexes on the {1 1 1} crystallographic face of magnetite referred to as species (i) in the text. The best-fit model based on our EXAFS fit results at the As K-edge suggests tridentate hexanuclear corner-sharing complexes (^{3}C) occur, giving As–Fe distances from (A) to (G) that are listed in Table 2. FeO_6 octahedra and FeO_4 tetrahedra are represented as shaded polyhedra. The AsO_3 pyramid is represented by a sphere corresponding to the As atom and by gray lines symbolizing the As–O bonds.

tion. According to such a hypothesis, a lower number of magnetite nuclei would be available for crystal growth in the presence of arsenic. Such an effect is, however, expected to favor the formation of bigger particles, provided that a large fraction of the arsenic will adsorb on a small fraction of the magnetite nuclei. Such a situation might be reached at low initial As(III) concentration (samples MtAs0.007 and MtAs0.033), in which case a small fraction of the arsenic might be left in solution after the nucleation step. This hypothesis is consistent with the observation that magnetite particles in samples MtAs0.007 and MtAs0.033 are slightly larger than those in the As-free one (sample MtAs0).

In contrast, at higher arsenic concentrations, a significant fraction of the initial arsenic is left in solution after the nucleation step, and thus can sorb onto the surface of magnetite particles during crystal growth. Adsorption of As(III) onto Mt {1 1 1} surfaces, as indicated by EXAFS analysis (species (i)), is expected to inhibit the growth of the magnetite particles. Indeed, arsenic sorption should decrease the interfacial tension, which is a driving force tending to increase particle size (Jolivet et al., 1994). In addition, the formation of an amorphous surface precipitate (species (ii)) at high initial arsenite concentration, could also inhibit the growth of magnetite particles by limiting the diffusion of the solute species toward the surface. The magnetite particles in the arsenic-rich systems will thus be smaller than in the arsenic-free system. Similar findings have been shown when arsenate is adsorbed onto ferrihydrite: the presence of arsenate during coprecipitation of two-line ferrihydrite results in a reduction in crystallite-size as a result of inner-sphere complexation of arsenate onto adjacent edge-sharing $Fe(O,OH)_6$ octahedra. (Waychunas et al., 1996).

4.3. Implications for As(III) solubility at the magnetite–water interface

The final concentration of dissolved arsenite in our magnetite synthesis experiments was found to regularly increase with increasing initial arsenite concentration (Table 1). However, more than 99.7% of the initial arsenic pool is sorbed by the solid phase for all samples, except for the most concentrated one (MtAs0.333). For this sample, in which As(III) is dominantly hosted by an amorphous surface precipitate (species (ii)), only 71.8% of the initial arsenic pool is sorbed by the solid phase. Such values of arsenic uptake can be interpreted by invoking both adsorption and precipitation, with the later process becoming dominant at the highest arsenite concentration (sample MtAs0.333). Apparent arsenite surface coverage, estimated from surface area values and from dissolved arsenic concentrations, is 0.8 ± 0.1 μmol m^{-2} for the most dilute sample (MtAs0.007), and it reaches a maximum value of 4.0 ± 0.2 μmol m^{-2} for all other samples (Table 1). This maximum value is slightly higher than the value of 3.7 μmol m^{-2} (i.e. a site density of 2.31 sites nm^{-2}) generally reported for arsenite sorption on iron oxides, including magnetite (e.g., Dixit and Hering, 2003). Such a high maximum surface coverage (4.0 ± 0.2 μmol m^{-2}) observed in our samples is, however, consistent with adsorption complexes of As(III) at the surface of magnetite particles. Indeed this maximum value is lower than the theoretical maximum site density (5.3 μmol m^{-2} or 3.2 sites nm^{-2}) of tetrahedral vacancies on the {1 1 1} magnetite surface with octahedral Fe terminations, which are the dominant sorption sites (^{3}C surface complex); it is also lower than the theoretical maximum density of sites available for ^{2}C complexes on the {1 0 0} magnetite surface (4.7 μmol m^{-2} or 2.8 sites nm^{-2}). However, this high apparent surface coverage could also be explained by the presence of the amorphous precipitate coating magnetite particles observed by HRTEM in samples with As/Fe ratios of 0.067 and above.

Finally, the high solubility of this amorphous surface precipitate, as shown by the elevated final dissolved arsenic concentrations in the synthesis experiments for samples MtAs0.133 and MtAs0.333 (Table 1), suggests that it may not represent a relevant species in natural systems unless the As(III) contamination levels of anoxic ground-water exceed the observed maximum of about 5000 μg/L, i.e., 66.67 μM (Smedley and Kinniburgh, 2002). In contrast, our results indicate that the ^3C $As(III)O_3$ surface complex

(species (i)), together with species (iii), plays a key role in lowering arsenite solubility in our experiments. Such species may thus play an important role in lowering the concentration of dissolved arsenite in putative magnetite-based water treatment processes (Yavuz et al., 2006), as well as in natural iron-rich anoxic media, especially during the reductive dissolution-precipitation of iron minerals in natural anoxic environments.

ACKNOWLEDGMENTS

The authors are indebted to the SSRL staff, especially John R. Bargar, Joe Rogers, and Samuel Webb as well as the SSRL Biotechnology Group, for their technical assistance during the XAS experiments. The three anonymous referees are acknowledged for their constructive comments that improved the quality of the manuscript. This work was supported by the ECCO/ECODYN CNRS/INSU Program, by ACI/FNS Grant #3033, by SESAME IdF Grant #1775 and by NSF-EMSI Grant CHE-0431425 (Stanford Environmental Molecular Science Institute). This is IPGP contribution # 2322.

REFERENCES

Ankudinov A. L., Ravel B., Rehr J. J. and Conradson S. D. (1998) Real-space multiple-scattering calculation and interpretation of X-ray-absorption near-edge structure. *Phys. Rev. B* **58**, 7565–7576.

Berar J. F. (1990) Reduction of the number of parameters in real time Rietveld refinement. IUCr. Sat. Meeting Powder Diffraction, Toulouse.

Cances B., Juillot F., Morin G., Laperche V., Alvarez L., Proux O., Hazemann J. L., Brown, Jr., G. E. and Calas G. (2005) XAS evidence of As(V) association with iron oxyhydroxides in a contaminated soil at a former arsenical pesticide processing plant. *Environ. Sci. Technol.* **39**, 9398–9405.

Choi B., Nelson C., Tsunashima Y. and Balter P. (2007) Open source, ImageJ based, web accessible tool for treatment plan evaluation. *Med. Phys.* **34**, 2477.

Coker V. S., Gault A. G., Pearce C. I., vanderLaan G., Telling N. D., Charnock J. M., Polya D. A. and Lloyd J. R. (2006) XAS and XMCD evidence for species-dependent partitioning of arsenic during microbial reduction of ferrihydrite to magnetite. *Environ. Sci. Technol.* **40**, 7745–7750.

Cooper D. C., Picardal F., Rivera J. and Talbot C. (2000) Zinc immobilization and magnetite formation via ferric oxide reduction by Shewanella putrefaciens 200. *Environ. Sci. Technol.* **34**, 100–106.

Cornell R. M. and Schwertmann U. (2003) *The Iron Oxides: Structure, Properties, Reactions, Occurrences and Uses*. Wiley-VCH Verlag GmbH & Co, Weinheim, Germany.

Devouard B., Posfai M., Hua X., Bazylinski D. A., Frankel R. B. and Buseck P. R. (1998) Magnetite from magnetotactic bacteria: size distributions and twinning. *Am. Mineral.* **83**, 1387–1398.

Dixit S. and Hering J. G. (2003) Comparison of arsenic(V) and arsenic(III) sorption onto iron oxide minerals: implications for arsenic mobility. *Environ. Sci. Technol.* **37**, 4182–4189.

Faivre D., Agrinier P., Menguy N., Zuddas P., Pachana K., Gloter A., Laval J. Y. and Guyot F. (2004) Mineralogical and isotopic properties of inorganic nanocrystalline magnetites. *Geochim. Cosmochim. Acta* **68**, 4395–4403.

Faivre D., Menguy N., Guyot F., Lopez O. and Zuddas P. (2005) Morphology of nanomagnetite crystals: Implications for formation conditions. *Am. Mineral.* **90**, 1793–1800.

Glasauer S., Weidler P. G., Langley S. and Beveridge T. J. (2003) Controls on Fe reduction and mineral formation by a subsurface bacterium. *Geochim. Cosmochim. Acta* **67**, 1277–1288.

Gloter A., Douiri A., Tence M. and Colliex C. (2003) Improving energy resolution of EELS spectra: an alternative to the monochromator solution. *Ultramicroscopy* **96**, 385–400.

Golden D. C., Ming D. W., Morris R. V., Brearley A., Lauer H. V., Treiman A. H., Zolensky M. E., Schwandt C. S., Lofgren G. E. and McKay G. A. (2004) Evidence for exclusively inorganic formation of magnetite in Martian meteorite ALH84001. *Am. Mineral.* **89**, 681–695.

Hansel C. M., Benner S. G. and Fendorf S. (2005) Competing Fe(II)-induced mineralization pathways of ferrihydrite. *Environ. Sci. Technol.* **39**, 7147–7153.

Hansel C. M., Benner S. G., Neiss J., Dohnalkova A., Kukkadapu R. K. and Fendorf S. (2003) Secondary mineralization pathways induced by dissimilatory iron reduction of ferrihydrite under advective flow. *Geochim. Cosmochim. Acta* **67**, 2977–2992.

Hill R. J., Craig J. R. and Gibbs G. V. (1979) Systematics of the spinel structure type. *Phys. Chem. Miner.* **4**, 317–339.

Horneman A., Van Geen A., Kent D. V., Mathe P. E., Zheng Y., Dhar R. K., O'Connell S., Hoque M. A., Aziz Z., Shamsudduha M., Seddique A. A. and Ahmed K. M. (2004) Decoupling of As and Fe release to Bangladesh groundwater under reducing conditions. Part 1: evidence from sediment profiles. *Geochim. Cosmochim. Acta* **68**, 3459–3473.

Hug S. J. and Leupin O. (2003) Iron-catalyzed oxidation of arsenic(III) by oxygen and by hydrogen peroxide: pH-dependent formation of oxidants in the Fenton reaction. *Environ. Sci. Technol.* **37**, 2734–2742.

Jolivet J.-P., Froidefond C., Pottier A., Chaneac C., Cassaignon S., Tronc E. and Euzen P. (2004) Size tailoring of oxide nanoparticles by precipitation in aqueous medium. A semi-quantitative modelling. *J. Mater. Chem.* **14**, 3281–3288.

Jolivet J.-P., Henry M. and Livage J. (1994) *De la solution à l'oxyde: condensation des cations en solution aqueuse, chimie de surface des oxydes*. InterEditions, Paris.

Jolivet J.-P., Tronc E. and Chaneac C. (2002) Synthesis of iron oxide-based magnetic nanomaterials and composites. *C. R. Chim.* **5**, 659–664.

Larsen O. and Postma D. (2001) Kinetics of reductive bulk dissolution of lepidocrocite, ferrihydrite and goethite. *Geochim. Cosmochim. Acta* **65**, 1367–1379.

Lovley D. R., Stolz J. F., Nord G. L. and Phillips E. J. P. (1987) Anaerobic production of magnetite by a dissimilatory iron-reducing microrganism. *Nature* **330**, 252–254.

Mann S., Sparks N. H. C., Couling S. B., Larcombe M. C. and Frankel R. B. (1989) Crystallochemical characterization of magnetic spinels prepared from aqueous solution. *J. Chem. Soc. Faraday Trans.* **85**, 3033–3044.

Morin G., Rousse G. and Elkaim E. (2007) Crystal structure of tooeleite, $Fe_6(AsO_3)_4SO_4(OH)_4 4H_2O$, a new iron arsenite oxyhydroxysulfate mineral relevant to acid mine drainage. *Am. Mineral.* **92**, 193–197.

Ona-Nguema G., Abdelmoula M., Jorand F., Benali O., Géhin A., Block J.-C. and Génin J.-M. R. (2002) Iron(II,III) hydroxycarbonate green rust formation and stabilization from lepidocrocite bioreduction. *Environ. Sci. Technol.* **36**, 16–20.

Ona-Nguema G., Jorand F., Benali O., Abdelmoula M., Génin J.-M. R. and Block J.-C. (2001) Key role of the kinetics of γ-FeOOH bioreduction on the formation of Fe(II)–Fe(III) minerals. *Hyperfine Interact. (C)* **5**, 415–418.

Ona-Nguema G., Morin G., Juillot F., Calas G. and Brown, Jr., G. E. (2005) EXAFS analysis of arsenite adsorption onto two-line ferrihydrite, hematite, goethite and lepidocrocite. *Environ. Sci. Technol.* **39**, 9147–9155.

Petitto S. C., Tanwar K., Eng P., Ghose S. K., Toney M. F. and Trainor T. P. (2006) Structure and reactivity of hydrated magnetite (1 1 1) surface. *Abstr. Papers Am. Chem. Soc.* **231**, 91-GEOC.

Polizzotto M. L., Harvey C. F., Li G., Badruzzman B., Ali A., Newville M., Sutton S. and Fendorf S. (2006) Solid-phases and desorption processes of arsenic within Bangladesh sediments. *Chem. Geol.* **228**(1–3), 97–111.

Polizzotto M. L., Harvey C. F., Sutton S. R. and Fendorf S. (2005) Processes conducive to the release and transport of arsenic into aquifers of Bangladesh. *Proc. Natl. Acad. Sci. USA* **102**(52), 18819–18823.

Rose J., Flank A. M., Masion A., Bottero J. Y. and Elmerich P. (1997) Nucleation and growth mechanisms of Fe oxyhydroxide in the presence of PO_4 ions. 2. P K-edge EXAFS study. *Langmuir* **13**, 1827–1834.

Rose J., Manceau A., Bottero J. Y., Masion A. and Garcia F. (1996) Nucleation and growth mechanisms of Fe oxyhydroxide in the presence of PO_4 ions. 1. Fe K-edge EXAFS study. *Langmuir* **12**, 6701–6707.

Smedley P. L. and Kinniburgh D. G. (2002) A review of the source, behaviour and distribution of arsenic in natural waters. *Appl. Geochem.* **17**, 517–568.

Sun S. H. and Zeng H. (2002) Size-controlled synthesis of magnetite nanoparticles. *J. Am. Chem. Soc.* **124**, 8204–8205.

Tamaura Y., Chyo G. S. and Katsura T. (1979) Fe_3O_4 formation by the ferrite process—oxidation of the reactive $Fe(OH)_2$ suspension induced by sucrose. *Water Resour. Res.* **13**, 21–31.

Thomas-Keprta K. L., Bazylinski D. A., Kirschvink J. L., Clemett S. J., McKay D. S., Wentworth S. J., Vali H., Gibson E. K. and Romanek C. S. (2000) Elongated prismatic magnetite crystals in ALH84001 carbonate globules: potential Martian magnetofossils. *Geochim. Cosmochim. Acta* **64**, 4049–4081.

Tronc E., Belleville P., Jolivet J.-P. and Livage J. (1992) Transformation of ferric hydroxide into spinel by Fe^{II} adsorption. *Langmuir* **8**, 313–319.

Vanysek P. (1995) Electrochemical series. In *Handbook of Chemistry and Physics 76th Edition (1995–1996)* (ed. D. R. Lide). CRC Press Inc., Boca Raton, FL.

Vayssieres L., Chaneac C., Tronc E. and Jolivet J. P. (1998) Size tailoring of magnetite particles formed by aqueous precipitation: an example of thermodynamic stability of nanometric oxide particles. *J. Colloid Interface Sci.* **205**, 205–212.

Waychunas G. A., Fuller C. C., Rea B. A. and Davis J. A. (1996) Wide angle X-ray scattering (WAXS) study of two-line ferrihydrite structure: effect of arsenate sorption and counterion variation and comparison with EXAFS results. *Geochim. Cosmochim. Acta* **60**, 1765–1781.

Winterer M. (1997) XAFS—a data analysis program for materials science. *J. Phys. IV* **7**, 243–244.

Yavuz C. T., Mayo J. T., Yu W. W., Prakash A., Falkner J. C., Yean S., Cong L., Shipley H. J., Kan A., Tomson M., Natelson D. and Colvin V. L. (2006) Low-field magnetic separation of monodisperse Fe_3O_4 nanocrystals. *Science* **314**, 964–967.

Associate editor: Robert H. Byrne